# Guided wave topological energy method for quantitative evaluation of corrosion in metal plates and tubes

Thomas Monnier, Salah-Eddine Hebaz

# GUIDED WAVE TOPOLOGICAL ENERGY METHOD FOR QUANTITATIVE EVALUATION OF CORROSION IN METAL PLATES AND TUBES

**Thomas MONNIER** **Salah-Eddine HEBAZ**
INSA de Lyon, Université de Lyon, Laboratoire Vibrations Acoustique, F-69621 Villeurbanne, France
Thomas.Monnier@insa-lyon.fr

## ABSTRACT

Monitoring and controlling corrosion defects in metal components is a major challenge for various industries, such as nuclear or oil & gas. Guided ultrasonic waves have already shown great potential for the rapid characterization of this kind of damage in thin-walled structures, including in hard-to-reach areas.

The objective of this work is to apply the topological energy imaging method to ultrasonic waves guided in plates and tubes. Its applicability to the quantitative assessment of corrosion defects will be examined with a focus on determining defect contours and quantifying thickness loss, as the guided wave tomography methods would attempt to do.

The method is based on numerical models and experimental measurements. The propagation of ultrasonic waves is modelled in the time domain by finite elements. First, we simulate a corrosion thickness loss by introducing a calibrated defect in the form of a flat bottom hole (FBH). Then, a corrosion defect with a more realistic shape and an irregular profile in the depth is taken into account. The experimental validation is performed for an aluminium plate and a steel tube.

The presented results are obtained for monomodal propagation, using one of the fundamental Lamb modes. They show that it is possible to characterize the defect with a resolution in the order of one wavelength by optimizing the design of the sensor network.

## 1. INTRODUCTION

The monitoring and control of corrosion defects in metallic components is a major issue for various industries, such as petrochemical, nuclear, oil & gas, etc. Ultrasonic Guided Waves (UGW) have shown a potential for non-destructive testing (NDT) of these defects in thin-walled structures such as plates, shells and pipelines. In addition to their high sensitivity to internal defects, they have the advantage of rapid propagation over long distances and with very little dissipation, allowing inspection of large installations and hard-to-reach areas [1-2].

Over the last two decades, several inspection systems based on EGOs have been developed and are widely used today to inspect large industrial structures. However, these techniques, generally based on the principle of pulse-echo ultrasound, remain global and often qualitative. They may allow the detection and localization of corrosion defects without providing information on the shape and dimensions. The presence of an agent on site remains necessary to make an accurate assessment and provide the required information [3].

To overcome these limitations, the concept of Structural Health Monitoring (SHM), has been developed over the past 15 years. It consists in the automatic and continuous monitor the condition of a structure by a network of embedded sensors. It enables the observation of changes in the physical and/or geometric properties of the in-service structure. The application of an inverse transformation on all the acquisitions allows reconstructing the properties of the environment and determining the characteristics of the damage [4] [5].

The qualitative or quantitative tomographic reconstruction techniques found in the literature falls into two main categories. The first one is based on advanced signal processing techniques exploiting approximations underlying the physical phenomena related to wave propagation in the structure. The principle is to observe from different angles the variation of one or more parameters (attenuation, time of flight and/or phase shift) sensitive to inhomogeneity. Measurements are generally carried out for each element of a sensor array, which completely or partially surrounds the area to be inspected. Then, a processing of these measurements, according to a given approach, allows accentuating the characteristics of the damaged area. Among these approaches, we identified the top three sub-categories: ray tracing methods (example: the RAPID method [6-7], the analytical method of filtered back-propagation and the algebraic method [8-10]), wave physics-based methods (example beamforming [11] and diffraction tomography [Belanger 2010]) and an hybrid method (HARBUT method [12]).

The second main category is based on a model (numerical, analytical or semi-analytical), and consists in solving the wave equation by taking into account the difference between the response of the system in its healthy and defective state. In particular, we cite : the Full Waveform Inversion (FWI) method [13] and the topological imaging method [14-16]. The advantage of these methods lies in the direct consideration of complex effects such as diffraction and multiple scattering, which allows for improved resolution.

In this work, we are interested in this last category, precisely topological imaging. This relatively recent and promising technique is based on the adjoint method, initially developed for shape optimization problems encountered in applied mathematics. It consists in estimating a cost function of the difference between the results obtained by a direct numerical model of the

reference structure and the measurements made on the supposedly defective structure. The difference, containing the signature of the defect, is time-inverted and injected into the so-called adjoint model. An analysis of the simulated field, refocused on the echogenic zone, allows the topology of the model to be modified by inserting the proportioned virtual defects. The latter is used again to evaluate the deviation and in turn generate a modified model. This process is repeated until the cost function converges to local minimum where the adjoint model approaches the topology of the inspected structure (Figure 1).

Since its introduction in the field of NDT, several variants have been proposed in the literature. They differ mainly in the mathematical development associated with the analysis of the cost function (sensitivity formulas, gradient or topological derivative, energy, etc.) and the choice of the technique to solve the wave equation (numerical method in the time domain [17, 15], frequency domain [18, 14], or a semi-analytical method [16, 19]).

Among others, the Time Domain Topological Energy method (TDTE) is of great interest for guided wave reconstruction. It allows to take into account all the diffraction physics in a direct, simple and unrestricted way, regarding to the nature of the material (isotropic, anisotropic, or other) or to the dispersive and multimodal nature of UGW. It requires only one iteration while offering a reconstruction of heterogeneities with an improved signal-to-noise ratio. In addition, a reduced measurement set of transducers is sufficient to perform a reconstruction. It has been applied for the inspection of isotropic and composite solids with bulk waves using a linear transducer array [15]. Due to its ability to image impedance variations, the method has also been used for medical imaging of biological tissues with low impedance contrasts [20]. Very recently, it has been used for weld inspection [21].

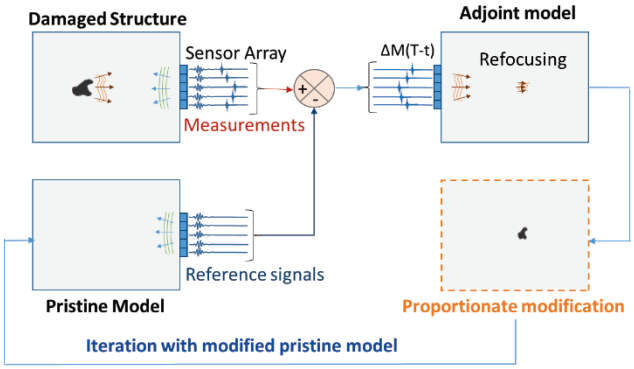


Figure 1. Principle of topological imaging.

However, until now, the TDTE can only provide qualitative information on defects. Therefore, the aim of this work is first to implement the TDTE method for guided waves in plates and tubes and second to focus on the quantitative aspects of the reconstructions of a corrosion defect. For this purpose, a standard defect in the form of a circular hole with a flat bottom is used. After this, a more complex shaped corrosion is modelled. The results of the numerical simulations are shown and discussed. Then, experimental results on homogeneous isotropic plates and tubes are exposed.

We presents a general description of the elastodynamic problem and the topological guided wave energy method in section 2. Then we expose the results of numerical simulations in section 3, while section 4 describes the experimental validation.

## 2. GUIDED WAVE TOPOLOGICAL IMAGING

In this section, we briefly present the fundamental propagation equations and the topological energy method. For more details on the mathematical developments of the latter, we refer the reader to the following references (see [14, 17, 18, 22, 23]).

### 2.1 Guided waves propagation

Consider a thin-walled elastic waveguide $\boldsymbol{\Omega}$ positioned in a Cartesian coordinate system $\mathbf{x} = (x1, x2, x3)$ and delimited by the external borders $\mathbf{S} = \partial\boldsymbol{\Omega}$. The propagation of elastic waves is governed by the general equation of motion resulting from the fundamental principle of dynamics [24] :

$$\rho \frac{\partial^2 \mathbf{u}}{\partial t^2} - \nabla \cdot \boldsymbol{\sigma}(\mathbf{u}) = \mathbf{f}, \qquad \mathbf{x} \in \boldsymbol{\Omega},\ t > 0 \qquad (1)$$

where $\rho$ is the density of the material, $\mathbf{u} = [u_1\ u_2\ u_3]^T$ is the displacement field, $\boldsymbol{\sigma}$ is the stress tensor, $\mathbf{f}$ are the volume forces and $t$ is time. The exponent T denotes the transposition. The stress tensor is expressed as a function of the displacement field via the generalized Hooke's law $\boldsymbol{\sigma}(\mathbf{u}) = \mathbf{C}\boldsymbol{\varepsilon}(\mathbf{u})$, where $\mathbf{C}$ denotes the tensor of the rigidities and $\boldsymbol{\varepsilon}(\mathbf{u}) = \frac{1}{2}(\nabla\mathbf{u} + \nabla\mathbf{u}^T)$ is the strain tensor.

Under the assumption of small linear deformations, the generation of waves of equal wavelength of the order of magnitude of the thickness generates guided waves that propagate in the axial direction. They are multimodal and dispersive. In the following, we consider thin-walled plates and tubes. We assume that propagation in a tube whose thickness does not exceed 10% of its radius of curvature is similar to wave propagation in a plate [25, 26, 27, 28, 29].

The Rayleigh Lamb equations have for solutions an infinite number of different propagative modes, all of which are dispersive.

The topological imaging method is based on the solution of two wave propagation problems. The principle is illustrated in Figure 1. The first step is to perform measurements on the damaged structure using an array of transducers placed on an edge $\Gamma_m \in \mathbf{S}$. These measurements $\mathbf{M}(\mathbf{x_m}, t)$ are conditioned by the nature of the excitation, the topology of the medium $\boldsymbol{\Omega}$ (including a possible defect), the boundary and initial conditions. The idea is to simulate this experiment under the same conditions (in particular the excitation) using a reference model $\boldsymbol{\Omega_0}$. This means solving the direct problem, which provides the displacement field and derived quantities at any point in the structure $\boldsymbol{\Omega_0}$. The principle of topological imagery is to describe a cost function that highlights the difference between the actual structure $\boldsymbol{\Omega}$ and the reference

structure $\boldsymbol{\Omega_0}$. Using the measurement of the displacement field $\mathbf{u_m}$ on the edge $\Gamma_m$, an intuitive cost function is written :

$$C(\boldsymbol{\Omega}, \boldsymbol{\Omega_0}) = \frac{1}{2}\int_0^T \left( \int_{\Gamma_m} | \mathbf{u} - \mathbf{u_m} |^2 \, \mathbf{dx} \right) dt \qquad (2)$$

To solve the inverse problem, this function should be minimized by introducing changes commensurate with the defect in the domain $\boldsymbol{\Omega_0}$ until it converges to $\boldsymbol{\Omega}$. However, this requires prior knowledge of the position of the defect. To get it, a topological sensitivity analysis (sensitivity of the cost function in relation to the location of the defect) is carried out.

In the direct problem, we simulate the experimental excitation to obtain a synthetic waveform corresponding to the propagation of the disturbance in the reference waveguide. The adjoint-problem method introduces a field $\mathbf{v}(\mathbf{x}, t)$ evolving with the time-inverted difference:

$$\boldsymbol{D_u} = -(\mathbf{u} - \mathbf{u_m})(\mathbf{x_m}, T - t) \qquad (3)$$

between the measured wavefield $\mathbf{u_m}$ and the one obtained via the direct problem $\mathbf{u}$, where T is the duration of the simulation.

The adjoint problem is a numerical time-reversal problem consisting in the retro-propagation of the signature of the defect (diffracted field) towards its source. By means of an array of transducers, refocusing creates a focal spot at the position of the defect. This summation of waves occurs at the same time as the direct field $\mathbf{u}(\mathbf{x}, t)$ interacts with the defect. Thus, the simplest idea to highlight the defect consists in calculating the product of the direct and adjoint fields. In this work, we will use the topological energy, defined by:

$$E(\mathbf{x}) = \int_0^T \| \mathbf{u}(\mathbf{x}, t) \|^2 \, \| \mathbf{v}(\mathbf{x}, T - t) \|^2 \, dt \qquad (4)$$

In the expression (4), the symbol $\| \cdot \|$ designates the Euclidean norm $\| \mathbf{u} \| = \sqrt{u_1^2 + u_2^2 + u_3^2}$. This quantity does not depend on the nature of the defect or the configuration of the simulation (2D or 3D), and provides neat results with good contrast and little oscillation, all this without iteration [15].

## 3. RESULTS

This section presents the implementation and numerical validation of the TDTE method. The modeling is performed on a commercial 3D finite element code for a plate with a calibrated defect. The results are shown and the applicability of the method for a first quantitative estimation is discussed.

### 3.1 Finite element modelling

Our time-domain propagation modelling is performed using– Abaqus®/Explicit package. It uses an based on a centred finite difference operator. Calculation results are extracted by Python scripts and post-processing is performed using Matlab®.

Figure 2 shows the schematic of the instrumented damaged plate, the so-called *experimental* model. Table 1 gathers the elastic properties of the carbon steel plate under consideration. The plate has a thickness H = 5 mm and dimensions (L = 400 mm, W = 400 mm). The corrosion defect is simulated by a circular flat-bottomed hole positioned in the centre of the plate, with diameter *d* and depth *p*. Figure 3 shows the dispersion curves of the phase velocity of the fundamental Lamb modes as a function of the frequency-thickness product [30]. The symmetrical mode is drawn as a dashed line and the antisymmetrical mode as a solid line. The hatched strip shows the working area. The excitation signal is a burst of 4.5 sinusoidal cycles of centre frequency $f_{ex}$ = 250 kHz, smoothed by a Gaussian window.

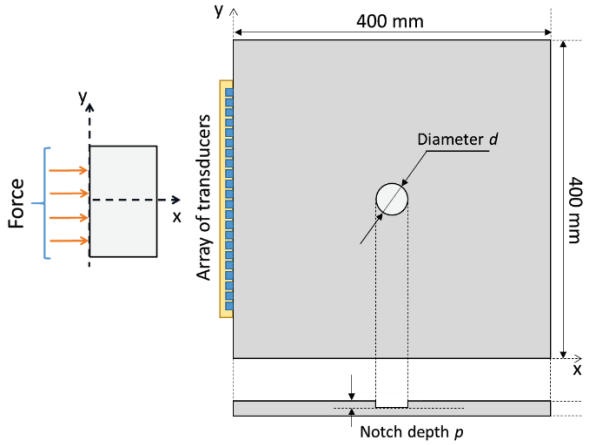


Figure 2. Schematic of the *experimental* model

The plate is discretized using linear three-dimensional cube-shaped elements (C3D8R). Material and digital damping effects are completely neglected. The stability of the numerical scheme only depends on the spatio-temporal discretization.

| | |
|---|---|
| Young's modulus | $E = 221$ GPa |
| Poisson coefficient | $\nu = 0.3$ |
| Density | $\rho = 7850 \text{ kg} \cdot \text{m}^{-2}$ |
| Longitudinal wave velocity | $c_L = 6156.1 \text{ m} \cdot \text{s}^{-1}$ |
| Shear wave velocity | $c_T = 3290.6 \text{ m} \cdot \text{s}^{-1}$ |

**Table 1.** Elastic properties of the carbon steel.

In order to meet the recommended minimum requirements [31], the minimum characteristic size of an element is set at $\Delta x = 1.25 \text{ mm} \leq c_T/10 f_{ex}$ with a time increment $\Delta t = 0.08 \text{ µs} \leq \Delta x/c_L$.

The transducer array is placed on an edge of the plate. In this configuration, the symmetrical fundamental lamb mode $S_0$ is solely generated [32]. This mode is commonly used for thickness loss control since it has the advantage of being fast (high group velocity in the working zone), sensitive to asymmetrical internal defects and very little attenuated [33, 34]. Moreover, its interaction with the standard defect is widely studied in the literature [35]. Working at the frequency $f_{ex}$, the group velocity is

$c_g = 5600$ m.s$^{-1}$ and the wavelength is $\lambda = 20$ mm. The simulations are calculated for a duration T = 200 µs, which corresponds to the time of the return of the reflection on the edge.

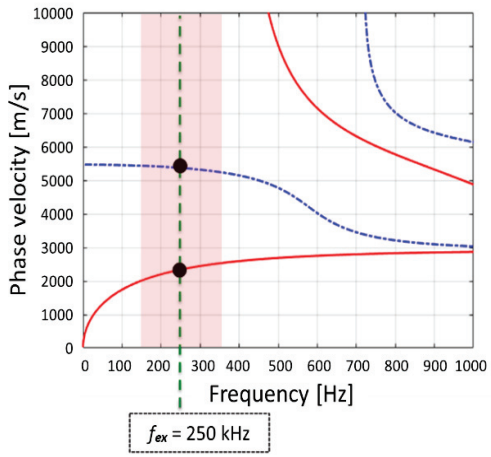


Figure 3. Dispersion curves of the phase velocities of Lamb waves in a 5mm-thick carbon steel plate.

The linear transducer array is composed of $n_t = 64$ elements of unitary length $l_t = 3$ mm. The distance between two adjacent elements is $d_t = 3$ mm. Since piezoelectric elements are not available in Abaqus®/Explicit, the transducer is simulated by a surface tension of magnitude T = 10 N/m$^2$. Furthermore, in order to save calculation time and increase efficiency, the transducer is simplified to "Integrated Output" at a point on the plate, so the output is the only displacement instead of every stress components for each element of the transducer.

In order to simulate the Lamb wave emission by a multi-element array, it is assumed that the excitation of the transmitter applies a surface traction perpendicular to the plate surface only. For reception it is assumed that the transducer is sensitive to out-of-plane displacements of the plate surface only.

The experiments consist of triggering all the elements of a linear array synchronously and recording the scattered field on each channel individually. The array is coupled to the plate along its edge so that the transducers are sensitive to in-plane motion (Figure 2, detail).

To obtain an image, the FE model is executed with and without defects, the defect-free case being used as the incident field and the case of the damaged plate being used to produce the “numerical measurements” to mimic those one could get from an actual experimental set of measurements. The magnitude of the topological energy is then calculated for any node of the plate reference model, but for clarity, we will represent it only in the midplane of the plate. Results obtained for a plate are also valid for thin and large diameter tubes, for which the effect of curvature can be neglected [29].

### 3.2 Towards quantitative topological imaging

The objective of this work is to study the possibility of using the topological energy method in guided waves for a quantitative evaluation of a corrosion defect in plates and tubes, *i.e* for the determination the defect contours and the quantification of thickness loss.

It is important to note that topological energy still exhibits oscillating behaviour, even if it is weak, because the convolution of two oscillating signals is an oscillating signal. Indeed, when the wave packets of the direct and adjoint fields, propagating in opposite directions, cross each other near and through defects, the topological gradient takes the form of a wavelet at the crossing point. Although it has an oscillatory character, an image of the defects in $\boldsymbol{\Omega}$ can be obtained. To avoid oscillations, other formulae have been proposed, including the spatial envelope of the topological gradient [19] and the envelope normalized by the direct field [16].

Although [20] has shown that topological energy can be used to reconstruct the physical properties of the environment in the same way as tomographic approaches will do, we choose here to characterize the defects by extracting objective criteria from the observations of the distribution and amplitude of the topological energy images.

#### *3.2.1 Assessment of thickness loss of a single FBH*

To meet this need, a physical interpretation must be assigned to the reconstructed quantity. This has been achieved for medical imaging of biological tissues by reformulating topological energy according to reflection coefficients [20]. In this work, we will attempt to empirically correlate the values of topological energy in the region of interest, i.e. on a potential defect, with the thickness loss caused by this defect.

For this purpose, we perform a parametric study by varying two of the characteristics of a single FBH, centred in the middle of the area to be inspected. The diameter will vary from 5 to 40 mm in steps of 5 mm, and the thickness -loss will vary from 25 to 75% in steps of 25%. As illustrations, Figures 4 and 5 show, on the same colour scale, the topological energy images obtained respectively for an intermediate defect and for the most severe of this study.

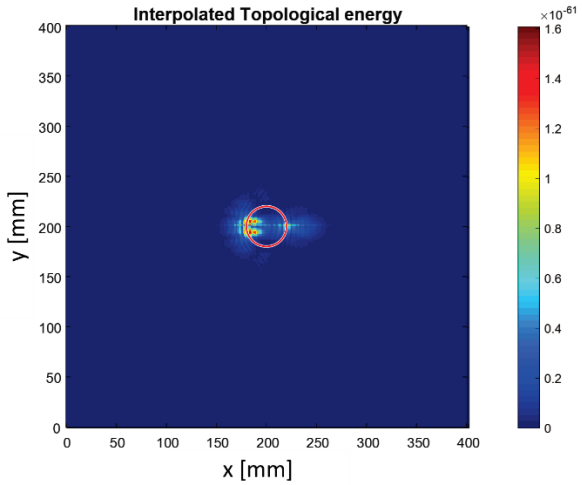


Figure 4. Topological energy for a flat-bottomed hole of diameter *d=20mm* and depth *p=H/4=1.25mm*

In terms of imaging, the actual shape of the defect is not put into evidence since only the edge of the defect that has been struck by the incoming wavefront is highlighted, and

to a lesser extent the opposite edge, while the side edges are almost invisible. Hence, we first focus on the maximum value of the topological energy as a function of the loss of thickness, for example for the two diameters shown here. Figure 6 shows a perfect quadratic adjustment, making it possible to make the link between the maximum of the topological energy and the percentage of loss of thickness, provided that we know the extent of the defect.

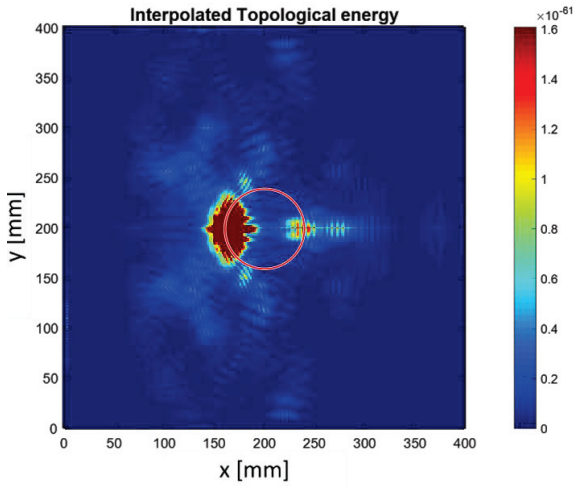


Figure 5. Topological energy for a flat-bottomed hole of diameter $d$=40mm and depth $p$=3$H$/4=3.75mm

One can also imagine having charts, also knowing that the magnitudes of topological energy obtained for an FBH of 40 mm in diameter are very exactly twice those obtained for an FBH of 20 mm in diameter.

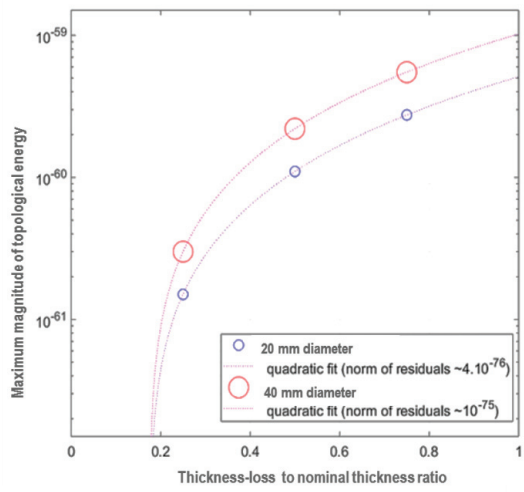


Figure 6. Maximum magnitude of topological energy as a function of thickness-loss for flat-bottom holes of diameter $d$=20 mm and $d$=40 mm

*3.2.2 Assessment of corrosion damage severity*

Nevertheless, one would be entitled to expect a simple criterion to judge the severity of corrosion damage. We therefore propose the notion of characteristic length $L_c$ as the ratio between the volume of the defect and its effective contact surface, i.e. for a flat-bottomed hole, the sum of the surface area of the disc representing the bottom and the circumferential surface of the cylindrical hole, leading to:

$$L_c = d\,H\,/(d + 4H)$$

Figure 7 shows the maximum topological energy as a function of the characteristic length of many damages with diameters ranging from 5 to 40 mm, and thickness-losses ranging from 25% to 75%. It can be seen that the data collected for from the simulations for all the configurations follow a master curve, which is approximated by a polynomial of fourth order.

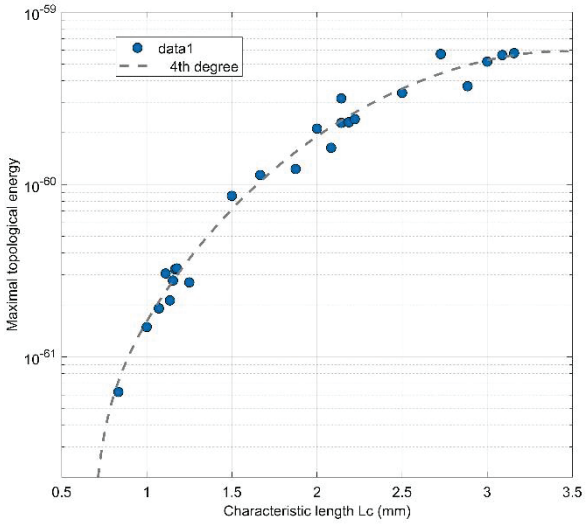


Figure 7. Maximum magnitude of topological energy as a function of the characteristic length of FBH

Thus, by simply measuring the maximum topological energy, we can quantify the severity of a corrosion defect by extrapolating from the case of a FBH.

### 3.3 Implementation of more complicated damage

*3.3.1 Illustration of masking effects with multiple FBH*

A second FBH is introduced to study the relative sensitivity to a reference defect T0 (diameter 20 mm, thickness-loss 50%) of one of the following three defects T1 to T3. The positions of the defects are shown in figure 8, which also shows the direction of the incident wavefront. The complete parametric study with diameters ranging from 5 to 40 mm, and thickness-losses ranging from 25% to 75% allowed us to draw the following conclusions.

For the T1 defect, which is far away from T0, we essentially observe a masking effect intrinsic to the method. This is due to the "attraction" of the topological energy by the predominant defect in the presence of several defects. The diameter criterion prevails over the depth of the defect. In case of equal severity (same diameter, same depth) it is the defect impacted first by the plane wave front that is better rendered.

As soon as fault T2 is behind T0 with respect to the incident wavefront, geometric masking occurs. The FBH

is only detected when its depth is greater than or equal to that of T0 and/or its diameter is greater than that of T0. It is only correctly rendered when both conditions are met simultaneously.

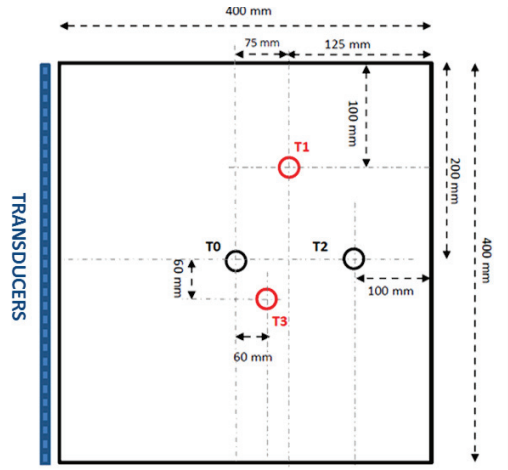


Figure 8. Arrangement of the FBH introduced separately and insonified from the left edge of the plate.

Unsurprisingly, as soon as the T3 defect is partially occulted by T0 during insonification, and all the more so as its diameter increases, we witness a combination of the two effects mentioned above. We will speak of mixed masking since the predominant effect of a larger diameter is here partially counterbalanced by the occultation due to the reference defect.

Finally, Figure 9 summarises these three assertions above, showing on a single image the merging of the indications obtained from three separate simulations of defects T1, T2 and T3 having all exactly the same characteristics as T0.

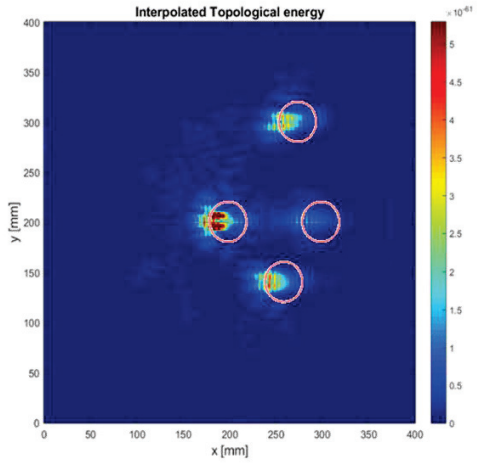


Figure 9. Composite image, merging three simulations

To overcome this limitation, we propose to carry out multiple successive tests, continuing to use plane wavefront insonifications, but with different directions of incidence, so as not to favour one defect more than another.

*3.3.2 Imaging of a defect with irregular shape*

Here we try to image a defect of irregular shape, centred in the area of interest but with an asymmetrical profile with a loss of thickness showing three different levels. Figure 10 (left) shows the reconstruction obtained by summing the topological energies from 4 simulations for which the insonification is done by a transducer strip placed on the left, top, right and bottom respectively, while the theoretical profile appears in figure 10 (right).

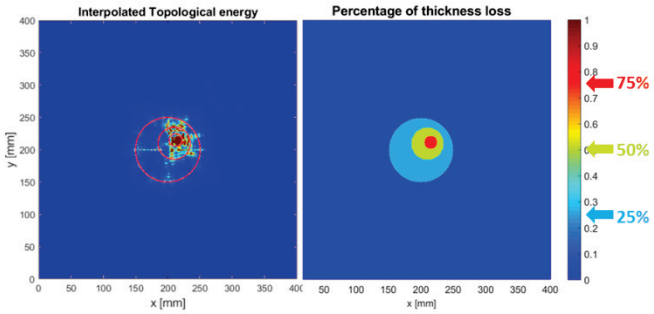


Figure 10. Topological imaging of an irregular defect. Sum of the results from 4 insonifications (left), expected thickness-loss image (right)

Having carried out multiple insonifications in different directions makes it possible to define the contours of this defect relatively well and in particular to qualitatively identify the most critical area.

### 3.4 Thinking about an experimental implementation

In the previous developments, the topological image is based on the fault signature $D_u$ obtained by subtracting the measured wave field u_m and the one obtained via the direct problem u. However, this requires that the reference model the structure $\mathbf{\Omega_0}$ as well as that of the transduction system (excitation and measurement) be as close as possible to the experimental conditions. However, even if the model is accurate, the simulation results cannot correspond perfectly to those obtained under normal experimental conditions; due to relatively unmanageable elements such as temperature change, surface state or transducer/structure coupling. The latter mainly influence the most energetic part of the signal, i.e. the excitation. A small error on this part is often energetic enough to hide the echo of the defect and generate dominant artefacts in the reconstruction.

On the other hand, from a theoretical point of view, the source term $D_u$ of the adjoint problem suggests that the adjoint field exactly simulates the field backscattered by the defect. However, the experimentally measured signals $M(x_m, t)$ actually correspond to one or a combination of the components of the velocity field and therefore do not allow the full complexity of the diffracted wave field to be taken into account. This poses a problem for guided waves in particular due to their multimodal nature and complex wave-damage interaction phenomena, including mode conversion and non-uniform scattering [24].

In order to overcome the limitations of the direct model, [36] proposes to perform measurements on a sound structure and then calculate the difference with the signals

obtained in a later state under similar experimental conditions. In addition, another approach without a reference state is possible. It consists in replacing the difference $D_u$ by the measured signals $M(x_m, t)$ while setting to zero the part corresponding to the excitation signal [20] [16].

Concerning the limitation of the measurement, the use of a real source term $D_u$ leads to an approximation of the solution of the adjoint problem. This is valid provided that $D_u$ is representative of the physical properties of the fault [16]. In principle, during guided wave diffraction, the energy of the incident wave is distributed between several reflected and transmitted modes, the amplitude of which is proportional to the characteristics of the defect. Therefore, the transduction system must take into account this transversality for each mode (sensitivity, excitability, detectability, etc.); this justifies the common use of a single-mode approach to simplify the analysis.

## 4. CONCLUSION

The present contribution was intended to test whereas guided ultrasonic waves have the potential to be used as carrier waves for the implementation of the topological energy imaging method in plates or tubes for the monitoring corrosion defects. We showed that it is possible to determine, to a certain extent, the contours of a defect. This could allow to determine the extent of the defect and, with the help of abacuses to quantify the thickness-loss, which is the main target characteristic.

By its very nature, the method is based on numerical models and experimental measurements. In this contribution, “experimental data” have also been simulated through time domain by finite elements modelling, in order to focus on the capability of the technique apart from experimental uncertainties linked to the bonding of sensors, changes in environmental conditions and so on. This allowed us to get results from the monomodal propagation of the fundamental symmetrical Lamb mode only, in presence of one or two flat bottom hole, and a corrosion defect with a more realistic shape. This allows us to identify ways of implementing an effective technique for the insonification of test pieces and for interpreting the results, for example in the presence of masking effects.

An ongoing work consists in implementing a series of experimental measurements, in order to compare the results of these simulations with those obtained in the real conditions of application of the method, i.e. with a set of data measured on a real structure using an array of piezoelectric transducers attached to its surface.


## ACKNOWLEDGEMENT

This research work is supported by the French National Agency for Radioactive Waste Management (ANDRA) as part of the Investissements d'Avenir Programme (PIA) and carried out at the National Institute for Applied Science in Lyon (INSA de Lyon).


## 5. REFERENCES


[1] D. N. Alleyne, B. Pavlakovic, M. J. S. Lowe, and P. Cawley, Rapid, long range inspection of chemical plant pipework using guided waves, *AIP Conference Proceedings* 557, 180, 2001.

[2] A. Demma, P. Cawley, M. Lowe, A. G. Roosenbrand B. Pavlakovic, The reflection of guided waves from notches in pipes: a guide for interpreting corrosion measurements, *NDT & E International,* Volume 37, Issue 3, pp. 167-180, 2004.

[3] A.Ghavamian, F. Mustapha, B. Baharudin, N. Yidris, Detection, Localisation and Assessment of Defects in Pipes Using Guided Wave Techniques: A Review, *Sensors* 2018 Dec 17;18(12). pii: E4470.

[4] Raghavan A and Cesnik C E S 2007 *Review of guided wave structural health monitoring Shock and Vibration Digest* 39, 91–114

[5] Zhao X, Royer R L, Owens S E and Rose J L, 2011, Ultrasonic Lamb wave tomography in structural health monitoring, *Smart Mater. Struct*. 20 105002

[6] Gao H, Shi Y and Rose J L, Guided wave tomography on an aircraft wing with leave in place sensors *Rev. Prog. QNDE*, AIP Proc. 760 1788–94, 2005.

[7] T R Hay, R L Royer, Huidong Gao, Xiang Zhao and J L Rose, A comparison of embedded sensor Lamb wave ultrasonic tomography approaches for material loss detection, *Smart Materials and Structures*, Volume 15, Number 4, 2006.

[8] A. Kak and M. Slaney, Principles of Computerized Tomography Imaging. Piscataway, NJ : IEEE Press, 1988.

[9] P. McKeon and M. K. Hinders, Parallel projection and crosshole Lamb wave contact scanning tomography, *J. Acoust. Soc. Am*. 106(5), 2568 (1999)

[10] E. V. Malyarenko and M. K. Hinders, Fan beam and double crosshole Lamb wave tomography for mapping flaws in aging aircraft structures, *J. Acoust. Soc. Am*. 108, 1631 (2000)

[11] R. Sicard, J. Goyette, D. Zellouf, A SAFT algorithm for lamb wave imaging of isotropic plate-like structures, *Ultrasonics* 39 (2002) 487–494.

[12] P. Huthwaite, F. Simonetti, High-resolution guided wave tomography, *Wave Motion* Vol.50, N°5, pp. 979–993, 2013.

[13] Rao, J.; Ratassepp, M.; Fan, Z. Guided wave tomography based on full-waveform inversion. *IEEE Trans. Ultrason. Ferroelectr. Freq. Control* 2006, 63, 737–745

[14] M. Bonnet and B. B. Guzina. Sounding of finite solid bodies by way of topological derivative. *Intern. Journ. for numerical methods in engineering*, 61, 2344-2373, 2004.

[15] N. Dominguez, V. Gibiat, Non-destructive imaging using the time domain topological energy method, *Ultrasonics* 50 (2010) 367–372.

[16] S. Rodriguez, M. Deschamps, M. Castaings, E. Ducasse, Guided wave topological imaging of isotropic plates, *Ultrasonics* 54 (2014) 1880–1890.

[17] N. Dominguez, V. Gibiat, Y. Esquerre, Time domain topological gradient and time reversal analogy: an inverse method for ultrasonic target detection, *Wave Motion* 42 (2004) 31–52.

[18] M. Bonnet, *Comptes Rendus Mécanique*, Vol. 338, Issues 7–8, pp 377-389, Inverse problems, Topological sensitivity of energy cost functional for wave-based defect identification, 2010.

[19] Samuel Rodriguez, Perrine Sahuguet, Vincent Gibiat, Xavier Jacob, Fast topological imaging, *Ultrasonics* 52 (2012) 1010–1018.

[20] P. Sahuguet, Imagerie ultrasonore de fantômes biologiques par optimisation topologique. *Thèse de doctorat*, Université de Toulouse III - Paul Sabatier, 2012.

[21] E. Lubeigt, Imagerie topologique de domaines élastiques bornés : application au contrôle non destructif des soudures, *Thèse de doctorat Acoustique*, Aix-Marseille 2017.

[22] B. Guzina, M. Bonnet, Topological derivative for the inverse scattering of elastic waves, *Q. Jl Mech. Appl. Math.*, 57, 161–179 (2004).

[23] S. Amstutz, N. Dominguez, Topological sensitivity analysis in the context of ultrasonic non-destructive testing, *Eng. Anal. Bound. Elem*. 32 (2013) 936–947.

[24] B.A. Auld, Acoustic Felds and Waves in Solids, vol. 1, *Wiley*, New York, 1973

[25] B.C. L. Willey, F. Simonetti, P. B. Nagy and G. Instanes, Guided wave tomography of pipes with high order helical modes, *NDT & E International*, Vol. 65, pp. 8-21, 2014.

[26] M. Ratassepp, A. Klauson, Curvature effects on wave propagation in an infinite pipe, ISSN 13922-2114 *ULTRAGARSAS*, Nr.2(59). 2006.

[27] M. G. Silk. And K. Bainton, The Propagation in Metal Tubing of Ultrasonicwave Modes Equivalent to Lamb Waves. *Ultrasonics*, 17, 11-19, 1979.

[29] J. Fong and M. Lowe, "Curvature effect on the properties of guided waves in plates," in Review of *Progress in Quantitative Nondestructive Evaluation*, 2004, vol. 23, pp. 126–133.

[30] Salah-Eddine Hebaz, Farouk Benmeddour, Emmanuel Moulin, Jamal Assaad, Semi-analytical discontinuous Galerkin finite element method for the calculation of dispersion properties of guided waves in plates, *The Journal of the Acoustical Society of America*, Vol.143, N.1, pp 460-469, 2018.

[31] I Bartoli, FL di Scalea, M Fateh, E Viola, Modeling guided wave propagation with application to the long-range defect detection in railroad tracks*, Ndt & E International*, 2005.

[32] Paul D. Wilcox, A Rapid Signal Processing Technique to Remove the Effect of Dispersion from Guided Wave Signals, *IEEE transactions on ultrasonics, ferroelectrics, and frequency control*, vol. 50, no. 4, april 2003 419

[33] O. Diligent, T. Grahn, A. Boström, P. Cawley and M. J. S. Lowe, The low-frequency reflection and scattering of the S0 Lamb mode from a circular through-thickness hole in a plate: Finite Element, analytical and experimental studies, *The Journal of the Acoustical Society of America* 112, 2589, 2002.

[34] F. B. Cegla, A. Rohde, M. Veidt, Analytical prediction and experimental measurement for mode conversion and scattering of plate waves at non-symmetric circular blind holes in isotropic plates, *Wave Motion*, Volume 45, Issue 3, pp. 162-177, 2008.

[35] T. Grahn, Lamb wave scattering from a circular partly through-thickness hole in a plate, *Wave Motion,* Volume 37, Issue 1, pp. 63-80, 2003.

[36] N. Dominguez, Modélisation de la propagation ultrasonore en milieu complexe – Application au contrôle non destructif et à la caractérisation de la porosité dans les matériaux composites stratifiées. *Thèse de doctorat*, Université de Toulouse III – Paul Sabatier, 2006.